Simultaneous maximum a-posteriori reconstruction of attenuation and activity distributions from emission sinograms.

Johan Nuyts[1]
Patrick Dupont[1]
Sigrid Stroobants[1]
Roel Benninck[1]
Luc Mortelmans[1]
Paul Suetens[2]

[1] Department of Nuclear Medicine,K.U. Leuven, Belgium
[2] ESAT-Machine Intelligence and Imaging, K.U. Leuven, Belgium
The research is supported by the Flemish Fund for Scientific Research (FWO), grant number G.0106.98. P. Dupont is a post-doctoral researcher of the "Fonds voor Wetenschappelijk Onderzoek (FWO)", Belgium.

IEEE Trans Med Imaging, 1999; 18 (5): 393-403.

Correspondence: Johan Nuyts
Dept. of Nuclear Medicine
University Hospital Gasthuisberg
Herestraat 49, B3000 Leuven, Belgium
Tel: (32) 16.34.37.15, Fax: (32) 16.34.37.59
e-mail: Johan.Nuyts@uz.kuleuven.ac.be

Abstract

In order to perform attenuation correction in emission tomography, an attenuation map is required. We propose a new method to compute this map directly from the emission sinogram, eliminating the transmission scan from the acquisition protocol. The problem is formulated as an optimization task, where the objective function is a combination of the likelihood and an a-priori probability. The latter uses a Gibbs prior distribution to encourage local smoothness, and a multi-modal distribution for the attenuation coefficients. Since the attenuation process is different in positron emission tomography (PET) and single photon emission tomography (SPECT), a separate algorithm for each case is derived. The method has been tested on mathematical phantoms and on a few clinical studies. For PET, good agreement was found between the images obtained with transmission measurements and those produced by the new algorithm in an abdominal study. For SPECT, promising simulation results have been obtained for non-homogeneous attenuation due to the presence of the lungs.

keywords: Attenuation correction
PET
SPECT
maximum likelihood reconstruction

I. Introduction

For quantitative or semi-quantitative analysis in positron emission tomography (PET) and single photon emission tomography (SPECT), attenuation correction is mandatory. PET systems and recent SPECT systems are equipped with a transmission source, enabling direct measurement of the photon attenuation in a particular configuration. However, for several reasons, there is still considerable interest in attenuation correction in the absence of transmission measurements. Many currently installed SPECT systems do not support transmission scanning. In PET, the transmission measurement increases the study duration significantly. When the transmission measurement is carried out prior to injection, the patient needs to stay immobile until the end of the emission scan. This may include a long period in which actually no data are acquired because, for many clinical applications, the early dynamic behavior of the tracer is of little interest. On recent PET systems, this problem can be alleviated with post-injection transmission imaging, but even in this case, the transmission measurement may contribute significantly to the study duration.

For the reasons stated above, many techniques have been suggested to further reduce the transmission scan duration by using a priori knowledge during the reconstruction [23, 19, 6], or implicitly in image segmentation algorithms [16, 3, 28, 30]. Several authors propose techniques which completely eliminate the need for a transmission measurement in some applications. These techniques can be divided in two classes. One class of algorithms applies segmentation algorithms to the emission sinograms or uncorrected emission images to locate regions of approximately constant attenuation, to which predefined attenuation coefficients can be assigned [17, 28, 30, 24]. The other class of algorithms attempts to extract information on the attenuation coefficients directly from the emission data. This can be done by iterative inversion of the forward mathematical model as suggested by Censor et al. in 1979 [2], Manglos et al. [15] and Krol et al. [11] and Bronnikov (with an approximate linear model) [1], or by exploiting the consistency relations, which, in turn, are based on such a model. The latter approach was proposed by Natterer [20], and further explored by Welch et al. [29] and Moore et al. [18]. In this paper, we present a new approach of the second class, which attempts to iteratively invert the forward model using likelihood optimization. The method is inspired on our observation that the absolute likelihood of an MLEM (maximum likelihood expectation maximization [26, 12]) emission image is always higher when attenuation is taken into account, as compared to no attenuation correction.

In contrast to the methods proposed by Censor et al. [2] and Manglos et al. [15], the algorithm of Krol et al. [11] and our own algorithm use likelihood optimization, taking into account the Poisson nature of the data. Krol et al. [11] derived an EM algorithm to optimize the likelihood for simultaneous reconstruction of attenuation and activity from SPECT emission sinograms. In this work, we propose to extend that approach to a maximum-a-posteriori (MAP) algorithm by incorporating some a priori knowledge about the attenuation coefficients. In addition, we present algorithms for both PET and SPECT. Another related work is that by Clinthorne et al. [4], who developed an algorithm for joint ML estimation of attenuation and emission images based on an emission and a transmission measurement. The problem studied in this paper can be regarded as an extreme case, in which the transmission measurement provides no information at all.

Our method will be referred to as MLAA, which stands for Maximum Likelihood reconstruction of Attenuation and Activity.

We wish to emphasize the distinction between the approach and the actual implementation. In our opinion, the main contribution of this paper is to show that the emission data contain a surprisingly high amount of information about photon attenuation, and that with only moderate constraining useful attenuation maps can be produced in some clinical SPECT and PET applications. We have chosen a constrained ML-approach because it takes into account the Poisson nature of the data, and because it can be easily extended to include a-priori knowledge. In order to investigate this approach, we have developed a program which has been shown to be effective in multiple experiments. However, no attempt was made to optimize the implementation. It is expected that both the speed of the algorithm and the quality of its reconstruction can be further improved. Because the implementation affects the results, several appendices are included to describe implementation details.

II. Methods

Because the effect of photon attenuation is different in PET and SPECT, different algorithms had to be derived. In this work, only two-dimensional PET (PET detector rings separated by inter-slice septa) and parallel beam SPECT are considered, although extension to fully three-dimensional PET and different SPECT geometries is straightforward.

A. Positron emission tomography

The basic algorithm

In PET, attenuation is independent of position along the projection line, and the expected number of counts, given the activity and attenuation distribution can be written as:

$$r_i = a_i\, b_i \;\text{ with }\; a_i = e^{-\sum_k l_{ik}\mu_k} \;\text{ and }\; b_i = \sum_k c_{ik}\lambda_k \quad (1)$$

where r_i is the expected number of counts, μ_j is the linear attenuation coefficient at position j, λ_j is the activity at the same position, c_{ij} models the sensitivity of detector i to activity in j in absence of attenuation, and l_{ij} represent the effective intersection length of the projection beam with the volume represented by pixel j.

In this work, Compton scatter, random coincidences and finite resolution effects are ignored. Excluding terms not

dependent on μ_j or λ_j, the log-likelihood function is [26, 12]:

$$L(\vec{\lambda}, \vec{\mu}) = \sum_i \left(-r_i + y_i \ln r_i\right) \tag{2}$$

where $\vec{\lambda}$ denotes the vector $(\lambda_1 \ldots \lambda_J)$ and similarly for $\vec{\mu}$, and y_i is the measured sinogram.

When either $\vec{\lambda}$ or $\vec{\mu}$ are known, the function L is concave in the other variable [26, 12]. However, this is no longer the case when both are treated as unknown. Finding the global maximum under these conditions requires very computationally intensive optimization strategies such as simulated annealing [7]. Consequently, we will limit ourselves to developing an algorithm which converges towards a local optimum. By inclusion of some a-priori knowledge, we attempt to ensure that that local optimum corresponds to a useful solution.

We propose a successive optimization approach in which $\vec{\lambda}$ and $\vec{\mu}$ are updated alternately. Holding $\vec{\mu}$ at its current value reduces the problem to that in emission tomography. Consequently, the likelihood can be increased by applying a single iteration of the ML-EM routine [26, 12]:

$$\lambda_j^{\text{new}} = \frac{\lambda_j}{\sum_i a_i c_{ij}} \sum_i \frac{c_{ij} y_i}{b_i}. \tag{3}$$

Similarly, updating $\vec{\mu}$ keeping $\vec{\lambda}$ constant can be done with a single iteration of an ML algorithm for transmission tomography. Indeed, equation (1) holds for transmission tomography with an external source, because in PET, the effect of attenuation is independent of the position along the projection line. Because the EM approach does not produce a closed form expression for the update [12], several algorithms have been proposed [23, 19, 6]. For this work, we have used a simple but effective gradient ascent method [22] but other algorithms could be used:

$$\mu_j^{\text{new}} = \mu_j + \frac{\alpha_p}{N} \left(1 - \frac{\sum_i c_{ij} y_i}{\sum_i c_{ij} a_i b_i}\right). \tag{4}$$

N is the diameter of the reconstructed area, α_p is a relaxation coefficient and b_i is the total activity along detector line i (predicted from the current reconstruction image $\vec{\lambda}$), which plays the role of the blank scan in equation (4).

The resulting algorithm is a (scaled) gradient ascent algorithm, not an expectation-maximization algorithm. For the update of $\vec{\lambda}$, we used the ML-EM algorithm, which is a scaled gradient ascent algorithm [10]. The fact that it is also an expectation-maximization algorithm is advantageous, because this eliminates the need for computation of the step size, but it is not essential in our combined procedure.

Missing attenuation data

However, in contrast with a typical transmission scan, some b_i may have a very small value here. When b_i is very small or zero, the sinogram value y_i provides little or no information about the attenuation coefficients along the projection line i. This is because for small b_i, the difference between b_i and y_i can be attributed to Poisson noise, so an ML-algorithm has to assign a very small weight to such (b_i, y_i) pairs. In the extreme case of $b_i = y_i = 0$, the measurement provides no information at all about attenuation along i. The resulting uncertainty about the background attenuation increases the number of possible solutions and, most likely, also the number of local maxima.

The skin is heavily vascularized and for most study types, the tracer concentration in the blood does not decrease to zero during the study period. In addition, skin cells are metabolically active and will accumulate some metabolic tracers such as ^{18}F fluorodeoxyglucose (FDG). As a result, it is reasonable to assume that activity and attenuation are zero along a projection line with $y_i = 0$, since that projection line is not likely to intersect the patient body. This assumption is implemented by applying the algorithm (4) to the modified sinograms $\vec{b'}$ and $\vec{y'}$, where

$$\begin{aligned} b'_i = b_i \quad &\text{and} \quad y'_i = y_i \quad \text{if} \quad y_i \neq 0 \\ b'_i = B \quad &\text{and} \quad y'_i = B \quad \text{if} \quad y_i = 0 \quad \text{with } B > 0. \end{aligned} \tag{5}$$

In words: for projection lines with $y_i = 0$, both the measured value y_i and the predicted non-attenuated value b_i are set to an arbitrary value B, thus driving algorithm (4) towards a solution with zero attenuation along i. Since Poisson noise is assumed, this driving "force" increases with increasing B. B should not be set to too high a value, since in studies with poor statistics, y_i may become zero for projection lines intersecting the body.

B. *Single photon emission tomography*

The basic algorithm

The expected number of counts is given by

$$r_i = \sum_j c_{ij} \lambda_j e^{-\sum_\xi l_{i\xi,j} \mu_\xi} \tag{6}$$

$$l_{i\xi,j} = l_{i\xi} \text{ if the trajectory from position } j \text{ to detector } i \text{ intersects position } \xi \tag{7}$$

$$l_{i\xi,j} = 0 \text{ otherwise.}$$

The first step of the alternated optimization is similar as above: updating $\vec{\lambda}$ keeping $\vec{\mu}$ constant can be implemented as a single iteration of ML-EM:

$$\begin{aligned} \lambda_j^{\text{new}} &= \frac{\lambda_j}{\sum_i a_{ij} c_{ij}} \sum_i \frac{a_{ij} c_{ij} y_i}{\sum_\xi a_{i\xi} c_{i\xi} \lambda_\xi} \\ a_{ij} &= e^{-\sum_\xi l_{i\xi,j} \mu_\xi}. \end{aligned} \tag{8}$$

The second step, however, cannot be carried out by applying an ML-algorithm for transmission tomography. To our knowledge, the problem of finding $\vec{\mu}$ when the sinogram $\vec{y}$ and the activity distribution $\vec{\lambda}$ are given has not been solved for SPECT. In appendix A, a new gradient ascent ML-algorithm for this problem is derived. The resulting algorithm is given by

$$\mu_j^{\text{new}} = \mu_j + \frac{\alpha_s}{N \sum_i q_{ij}} \sum_i q_{ij} \left(1 - \frac{y_i}{\sum_\xi c_{i\xi} a_{i\xi} \lambda_\xi}\right) \tag{9}$$

$$q_{ij} = \sum_k c_{ik} a_{ik} l_{ij,k} \lambda_k. \quad (10)$$

Here, α_s is a relaxation factor. The weight q_{ij} can be interpreted as the total amount of photons that are detected in i and that had a trajectory intersecting position j: the value of q_{ij} is a measure for the influence of μ_j on the predicted value for y_i.

Missing attenuation data

As was the case for PET, the value y_i contains no information on attenuation when there is no activity along the projection line i. Since adapting (5) to SPECT does not yield a procedure of similar simplicity, a different approach is used. A temporary sinogram $\vec{z}$ is constructed and backprojected into an image $\vec{Z}$ as follows

$$\begin{aligned} z_i &= 1 \text{ if } y_i = 0 \text{ , and } z_i = 0 \text{ otherwise} \\ Z_j &= \frac{\sum_i c_{ij} z_i}{\sum_i c_{ij}}. \end{aligned} \quad (11)$$

The pixel value Z_j contains the fraction of projection lines with zero measured counts, contributing to j. Pixels with a value Z_j larger than a threshold are likely to belong to the background (assuming activity in the skin and in absence of noise, any non-zero value of Z_j would indicate that j is in the background). For those pixels, a small constant value is subtracted from μ_j in every iteration. This is equivalent to a prior distribution with log-likelihood proportional to $-\mu_j$. A good threshold must be determined experimentally. The resulting effect is that of driving the attenuation towards zero except within a wide hull containing nearly all of the activity in the image.

C. Prior distributions

Since a unique solution is not guaranteed, prior knowledge is incorporated in the algorithm in an attempt to guide it towards a meaningful solution. This knowledge only concerns the attenuation coefficients: 1) we expect to find only values typical for attenuation in tissue, air and possibly lungs, and 2) we expect the attenuation map to be locally smooth.

The a-priori knowledge about absolute attenuation values is implemented as a bi- or trimodal probability distribution. Incorporation of the prior knowledge can be regarded as a segmentation, since the algorithm continuously attempts to assign every reconstructed attenuation value to one of the modes of the prior. Intensity priors have been used previously in MAP-reconstruction, see e.g. [13, 14].

The local smoothing prior is implemented using a two-dimensional Gibbs-distribution [8, 19]. Details are provided in appendix B.

D. Initial images

It is obvious that this gradient approach only guarantees convergence towards a local optimum. Methods to find the global maximum, such as annealing [7] are too slow for this application. As a result, the final solution depends on the initial image and on the steps computed during the iterations.

To produce an initial attenuation map, the same algorithm used to compensate for missing information in SPECT is applied, both for PET and SPECT, with a more conservative threshold value. We compute the image $\vec{Z}$ with (11), and threshold it with 0.08 to produce a wide convex hull. The initial activity distribution is obtained by applying a few MLEM iterations using the initial attenuation map. After this, the ML-algorithms for activity and attenuation are applied alternately.

E. Projector-backprojector

Our projector-backprojector uses precomputed interpolation coefficients. We use "variable binning" [25] to reduce the storage requirements with a factor of about $N/2$, where N is the number of detectors [21]. This technique involves interpolation of sinogram lines into a finer grid. This causes a small amount of extra blurring, but because this blurring is less than that due to the limited camera resolution, it does not cause artifacts (in fact it makes the projector slightly more realistic). Since they use the same precomputed coefficients, the projector and backprojector are closely matched.

In our implementation, the coefficients c_{ij} and l_{ij} are identical (implying that the unit of length equals the pixel size, and that the diameter of the reconstructed area N equals the number of pixels in a row or column of the image). However, following Erdoğan et al [5], we use different symbols since these coefficients model different physical quantities.

F. Acceleration

As with MLEM, the MLAA algorithm can be accelerated using ordered subsets (OS) [9]. This has been implemented by replacing the summations over all projection lines i in the equations (3), (4), (8) and (9) by summations over a subset of projections lines. For the next sub-iteration, a different subset is selected until all subsets have been used. A sequence of sub-iterations in which all projections are used once is considered as a single OS iteration. The processing time consumed by an OS iteration is comparable to that of a regular MLAA iteration. Selection of the subset is done by maximizing the difference in projection angles with the previous subset. However, the priors are recomputed in every subiteration, and since their computational work depends on the image size, not on the subset size, that part of the calculation is not accelerated.

III. Experiments

A. Computing $\vec{\mu}$ from $\vec{\lambda}$ and the SPECT sinogram

An evaluation of the new algorithm (9) is required, in order to verify whether it is indeed capable of reconstructing the attenuation map from the known activity distribution and the SPECT sinogram. An elliptical object was simulated, with a constant activity and a Shepp-Logan phantom type of attenuation distribution. With the new algorithm (9) the attenuation distribution was reconstructed from the simulated sinogram and the known homogeneous tracer distribution.

In addition, the reconstruction was repeated, now replacing the true tracer distribution with a uniform random distribution, within the same object boundary.

B. Simulations

1) Non-convex homogeneous objects

Since both the SPECT and PET algorithms contain heuristics which tend to assign zero attenuation to pixels along projection lines with zero counts, both algorithms are rapid in producing an approximately convex hull of the body. Consequently, non-convex body outlines are needed to challenge the performance of the ML-algorithm. Therefore, two different and highly non-convex objects are simulated. Both objects were reconstructed with exactly the same set of parameters to obtain some information on the robustness of the algorithms. The same two objects were used for PET and SPECT, but with different image sizes. For SPECT, we used 50 detectors and 90 attenuated views over 360 degrees were computed, the resulting sinogram was reconstructed into images of 50x50 pixels. For PET, 100 detectors were used, 130 attenuated views over 180 degrees were computed and reconstructed into images of 100x100 pixels. No Poisson noise was added.

In all four simulations, the prior probability distributions used during reconstruction were centered at the actual attenuation value. Because the initial attenuation map tends to overestimate body size, transition from tissue to background attenuation is more likely to be needed than vice versa. To ease this transition, the standard deviation of the background prior was set 4 times wider than that of the tissue prior (so intermediate values are more attracted towards the background). For the Gibbs prior, the Geman function (Appendix B, eq. (25)) was used. In all cases, 1000 iterations without acceleration were applied.

2) Thorax simulation

A simplified thorax object, composed of ellipses, was simulated to study the behavior of the algorithm in the case when the object contains two different attenuation coefficients. Assuming a homogeneous background activity of 1, the myocardial activity was set to 5 and the activity of a small hot spot in the lung was set to 3. For PET, 130 views over 180 degrees were simulated, with 100 detectors per view. The tissue attenuation was set to 0.095 cm^{-1}, assuming a pixel size of 4 mm. For SPECT, 90 views over 360 degrees were simulated, with 50 detectors per view. Tissue attenuation was set to 0.125 cm^{-1}, assuming a pixel size of 5 mm. In both cases, lung attenuation was set to one third of tissue attenuation.

The prior distribution of attenuation coefficients now has three modes instead of two, which represents a significant increase in the number of degrees of freedom.

For the SPECT simulation, all three standard deviations of the prior distribution were simply set to the same value. For the PET simulation, useless results were obtained unless the width of the tissue prior was set much smaller than those of background and lung. The result shown later was produced by setting the width of the tissue prior to be one-tenth that of the other two.

C. Patient studies

The algorithm was only evaluated on clinical studies where a constant attenuation was an acceptable approximation: there were no lungs in the field of view and a bimodal prior was used (ignoring the higher uptake in bone relative to tissue). For clinical PET-studies, we used $\bar{\mu}_1 = 0$ and $\bar{\mu}_2 = 0.095$ cm^{-1} (value derived from transmission measurements in patients). For SPECT studies with ^{99m}Tc, we used $\bar{\mu}_1 = 0$ and $\bar{\mu}_2 = 0.125$ cm^{-1} (value used in clinical routine for calculated attenuation correction based on manual contours). For the corresponding standard deviations, we set $\sigma_1 = 4 * \sigma_2$. This was done to ease transition from tissue attenuation towards background attenuation. Indeed, as before, the initial attenuation boundaries are chosen too large, and therefore, more transitions from tissue to background values are needed than vice versa.

The MLAA algorithm was applied to the emission sinogram of an abdominal PET FDG-study. The sinogram was reconstructed using an accelerated iteration scheme, based on a decreasing number of projection subsets. The scheme was 1x64, 1x50, 1x40, 3x32, 3x16, 3x8 and 4x1, where the first figure denotes the number of OS iterations, and the second one the number of subsets. The prior protects the attenuation map against high frequency noise, but at high iteration numbers the unconstrained emission image is severely distorted by the well-known noise propagation. For visual inspection, the image is smoothed with a two-dimensional Gaussian mask with a standard deviation of 1 pixel.

The algorithm was also applied to a PET FDG study of the lower limbs, consisting of 150 planes, using the scheme 8x32, 3x16, 3x8 and 4x1.

The algorithm was used to reconstruct a series of SPECT ^{99m}Tc-HMPAO labeled white blood cell studies of patients suffering from inflammatory bowel disease.

The PET images were acquired on a ECAT931-08-15 [27], typical injected dose is 350 MBq. The SPECT images were acquired on a Trionix Triad systems, the dose was 180 MBq.

IV. Results

A. Parameter values

The method contains several heuristic parameters, to be tuned experimentally.

For the transmission reconstruction algorithm (4), we obtain good results with $\alpha_p = 2$. Convergence is slower for lower values, oscillations occur for values which are much higher.

For the corresponding relaxation factor α_s in (9), similar values are used.

For the value B in (5) good results are obtained for values in the order of $B = \text{mean}(\vec{b})/10$.

For SPECT, the threshold in (11) was set to 0.05 which tends to overestimate the object size. This is conservative, since it avoids driving object pixels towards background values, and leaves the detection of the final body outline entirely to the actual MLAA iterations.

B. Computing $\vec{\mu}$ from $\vec{\lambda}$ and the SPECT sinogram

The attenuation map reconstructed from the simulated emission distribution and the SPECT sinogram is compared to the original image in fig. 1. The same figure also shows that the likelihood increases as a function of the iteration number.

Figure 1: Left: Reconstruction of the attenuation map from a simulated sinogram and the known tracer distribution; Center: the original map. Right: The corresponding log-likelihood as a function of the iteration number.

When the iterations were carried out using the random distribution instead of the true distribution, the likelihood still increased monotonically. As expected, the likelihood was systematically lower and the reconstruction differed considerably from the true attenuation map.

C. Simulations

1) Non-convex homogeneous objects

Figure 2 shows the results obtained for the PET simulation after 1000 iterations. For comparison, the MLEM reconstruction without attenuation correction is also shown scaled to its own maximum (the mean value of the non-attenuation corrected images is lower by a factor of about 5). We found that in these noise-free simulations, the smoothness prior is not required. For convergence to a nearly exact solution, a bimodal prior favoring the two possible attenuation coefficients is sufficient. Note that there is some cross-coupling between attenuation and activity images: regions of high activity tend to have decreased attenuation coefficients (attenuation of the central ellipse is decreased by approximately 5%).

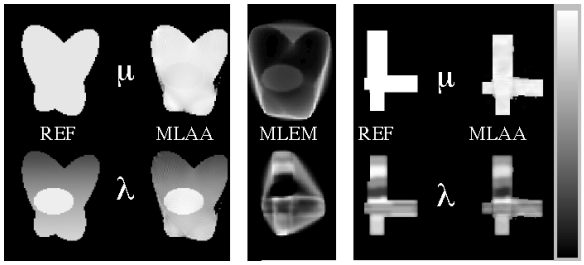

Figure 2: *Left panel:* MLAA reconstructions (1000 iterations) of the simulated PET sinogram for the first non-convex object. From left to right and top to bottom: the true attenuation map, the MLAA attenuation map, the true activity distribution and the MLAA reconstructed activity image. Reference and MLAA images are displayed with common gray scale. *Right panel:* same for the second object. *Center:* MLEM emission reconstructions without attenuation correction of first object (top) and second object (bottom), scaled to their own maxima (required for viewing).

Figure 3 shows the corresponding images for SPECT.

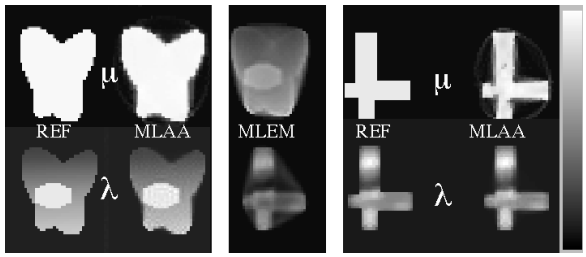

Figure 3: MLAA reconstructions (1000 iterations) of the simulated SPECT sinograms for both simulated non-convex objects. Layout and scaling as in figure 2.

2) Thorax simulation

Fig. 4 shows the MLAA reconstruction from the SPECT attenuated emission sinograms, for the case of three possible attenuation coefficients. Selection of parameters was not critical. The same figure also shows the corresponding PET reconstructions. Parameters have been tuned to produce reconstruction images in which the lungs were clearly visible.

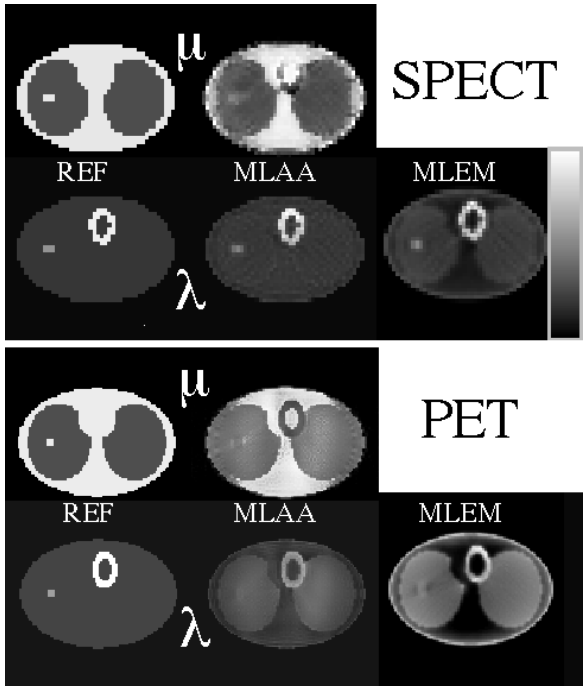

Figure 4: *Top panel:* MLAA reconstruction for the SPECT thorax simulation. From left to right and top to bottom: the true attenuation map, the MLAA attenuation map, the true activity distribution, the MLAA reconstructed activity image and the MLEM reconstruction without attenuation correction. Reference and MLAA images are displayed with common gray scale. The non-attenuation corrected image is scaled to its own maximum to make it clearly visible. *Bottom panel:* Same for the PET thorax simulation.

3) Convergence behavior

Fig. 5 shows the typical evolution of the (SPECT) attenuation map as the MLAA-iterations proceed. The initial attenuation map is, in the case of a single object, always a wide convex hull. In the concave regions, convergence is slowest at the boundaries, assignment of background attenuation proceeds from the center towards the edges. Even after 1000 iterations,

there is still a ring with non-zero attenuation near the boundary of the initial image. Similar behavior is observed for the other object, and also for the PET simulations and patient studies.

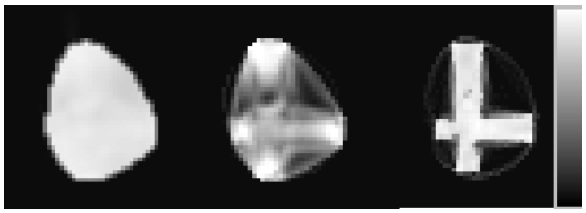

Figure 5: MLAA reconstructions at iteration numbers 1, 60 and 1000, for the SPECT-simulation of the second non-convex object.

D. Patient studies

In fig. 6 the reconstruction from a PET peritoneal metastases study is shown. The accelerated MLAA emission image is compared with attenuation corrected FBP and MLEM reconstructions, and the MLAA attenuation map with the FBP and ML reconstructions of the measured transmission scan. In addition, the non-attenuation corrected ML-images are shown.

The absolute difference between the emission images from MLAA and MLEM with measured attenuation correction reveals very good agreement: the difference image contains mainly noise. The mean squared error was determined using all pixels with significant attenuation in the MLAA map. It amounts to 28% of the mean or 6.5% of the maximum from the MLEM image. There is also a good agreement between the MLAA attenuation map and the ML-reconstructed transmission scan. The difference image shows small deviations at the body contour, and that the MLAA reconstruction does not contain the patient bed.

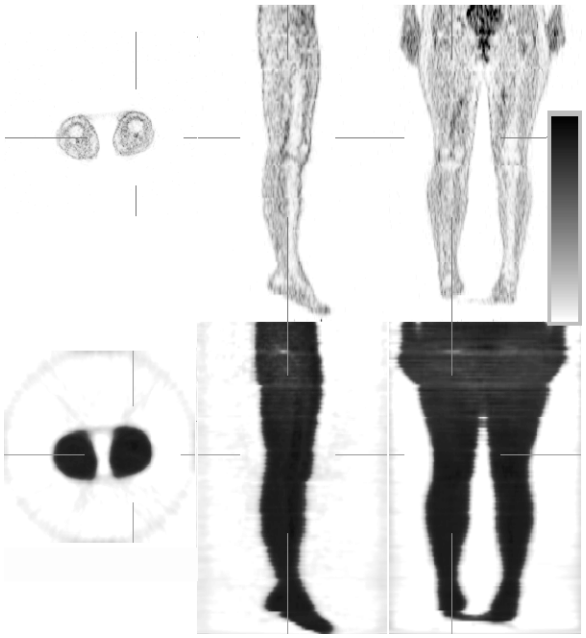

Figure 7: MLAA reconstruction of a PET study of the lower limbs (transaxial, sagittal and coronal sections through reconstructed activity and attenuation distributions).

Fig. 7 shows transaxial, sagittal and coronal slices of a FDG PET study of the lower limbs, reconstructed with accelerated MLAA. At our department, PET whole body studies are carried out without transmission scan in order to reduce the scan time to an acceptable duration. Consequently, there is no reference image to compare with and the images can only be evaluated visually.

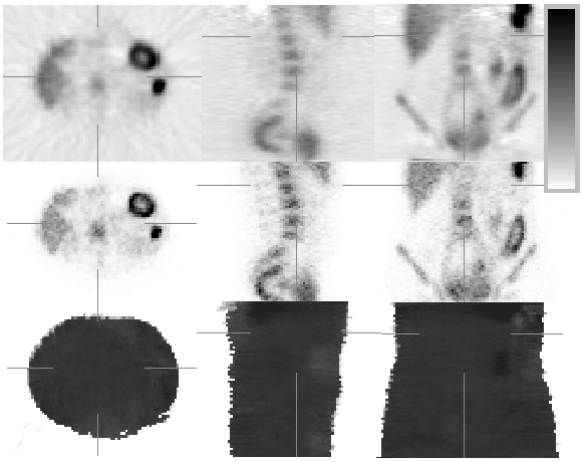

Figure 8: MLAA reconstruction of a SPECT ^{99m}Tc-HMPAO labeled white blood cells study of a patient with inflammatory bowel disease. Transaxial, sagittal and coronal sections through reconstructed activity and attenuation distribution. Top: FBP without attenuation correction, center: MLAA emission images, bottom: MLAA attenuation images.

Fig. 8 shows transaxial, sagittal and coronal slices of a SPECT ^{99m}Tc-HMPAO labeled white blood cells study of the abdomen. For comparison, the typical clinical reconstruction, produced with filtered backprojection (FBP) without attenuation correction, is also shown. Again, the images have to be judged by visual inspection because no transmission scan was available. However, with this tracer, the liver is expected to show homogeneous uptake, which is the case in the accelerated MLAA reconstruction.

V. Discussion

The aim of this work was to investigate whether ML-reconstruction of emission sinograms is capable of compensating for attenuation in the absence of a transmission scan. In order to do so, an ML-algorithm was developed by combining some existing algorithms, along with a new one, into a single procedure. This procedure is clearly heuristic and contains multiple parameters which influence the final result. This seems unavoidable, because the problem is probably highly under-determined, and the likelihood function does not contain a single maximum. Explicit heuristic parameters include the initial images, the weights of the priors, the choice of the cost function in the Gibbs prior and the relative size of the alternated optimization steps in solution space.

At this stage, we have not systematically investigated the influence of all these parameters. Our current feeling is that the parameter values are not critical for the case of constant attenuation in an arbitrarily shaped body. E.g. we found that the introduction of ordered subsets (which clearly affects

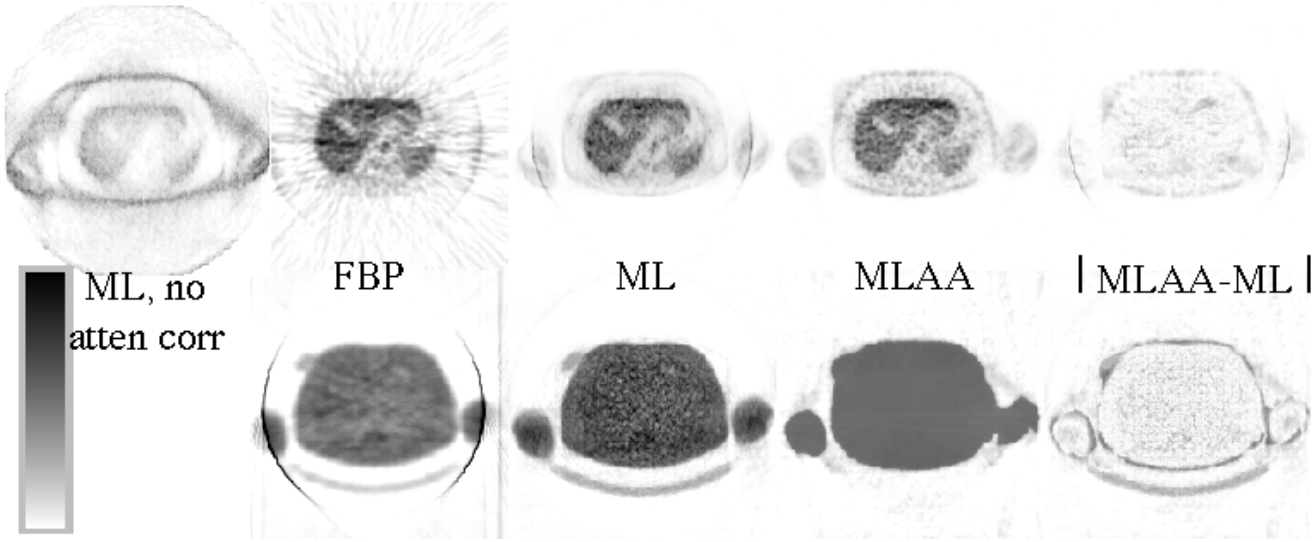

Figure 6: Reconstructions of an abdominal PET study. From left to right; top: MLEM without attenuation correction, FBP and MLEM with measured attenuation correction, MLAA emission image, absolute difference between MLAA and MLEM images. Bottom: FBP and MLEM reconstruction of PET transmission study, MLAA attenuation map, absolute difference between MLAA and ML attenuation maps. All emission images are displayed with the same grayscale, except the non-attenuation corrected MLEM image. All transmission images are displayed with the same grayscale. (The ring artifact is caused by truncation of the normalization near the edges, a problem solved in newer PET systems.)

the trajectory through solution space) did not compromise convergence in patient studies. In the noise-free simulations with a single non-zero attenuation, surprisingly good results have been obtained. In these simulations, the smoothness prior was not needed, and good results were obtained as long as the weight of the bimodal prior for absolute attenuation coefficients was low. (When that weight is set too high, the initial image becomes a local minimum from which no departure is possible.) Constraining the attenuation map with a bimodal distribution and a smoothing prior reduces the set of possible solutions. Moreover, MLAA rapidly produces a convex hull, effectively forcing many pixels from the attenuation map to zero, which further reduces the solutions set. Apparently, this reduction is sufficient to obtain acceptable images. This approach limits the applicability of the method to cases in which the tracer uptake near the skin is sufficiently high, such as in the reported patient studies.

In the case where the lungs are in the field of view, three different attenuators are present: air, lung and tissue. Consequently, the prior for absolute coefficients now shows three peaks, implying that the reduction of the set of solutions is not as strong as in the bimodal case, and that the risk of convergence towards an undesired solution is increased. In the case of SPECT, a reasonable MLAA reconstruction was obtained without tuning of the parameters. For PET, very poor results were obtained initially. Only after careful tuning the width of the priors the result of fig. 4 was produced. Here the lungs are visible in the attenuation map, but the reconstruction of heart and the hot spot in the lung is still unsatisfactory. In both cases, there is considerable “cross-talk” between the activity and attenuation images: to some extent, increased regional activity can be traded in for decreased regional attenuation. This cross-talk does not come as a surprise: since the likelihood function is not concave, the optimum activity value for a pixel is expected to depend on the values of surrounding pixels, and the trimodal constraint is not strong enough to exclude aberrant solutions. This ambiguity is more pronounced in PET than in SPECT. Manglos et al. [15] reported the same effect using a multiplicative ART-based iterative algorithm in SPECT.

We have not compared the performance of our method to that of the consistency method proposed by Welch et al. [29]. The consistency and the likelihood criteria are probably not as different as they may seem. A sinogram is consistent if it is identical to the reprojection of its reconstruction. This means that optimizing the consistency is equivalent to minimizing the difference between the measured projections and those calculated from the reconstruction. Similarly, the likelihood becomes maximum when measured and calculated projections are identical. The main difference in the methods is in the measure used to quantify the deviation between measured and calculated data.

In its current implementation, the consistency method [29] is used to optimize the shape of a parametric curve that represents the border of a homogeneous attenuator. Since only a few parameters are used to describe the curve, a very strong constraining is implicitly applied. In contrast, in our ML-approach a large number of parameters is used (the pixels of an image), and an explicit constraint is required. An explicit constraint gives better control, but it requires a larger amount of computations per iteration. As illustrated in fig. 5, assignment of background attenuation in concave regions always starts from the innermost part of the region, gradually moving towards the borders at higher iterations. This indicates

that the gradients near the borders are relatively small, which is a potential weakness of contour based methods.

Thresholding of the image computed with (11) is a segmentation method producing a first estimate of the body outline. This approach has some similarity to the sinogram segmentation method [17] and produces similar results on convex objects. Both methods fail in the case of non-convex object shapes. However, in contrast with the sinogram segmentation method, algorithm (11) is capable to delineate multiple convex objects in a single image, provided that they are well separated by the background. This is useful in some applications, such as studies of the lower limbs. We find that in applications where the body outline is convex, the algorithm (11) produces good attenuation maps, hardly modified by the subsequent MLAA iterations. Consequently, this algorithm can be directly combined with MLEM for emission into a relatively fast and clinically useful reconstruction procedure for such applications.

Tai et al. [28] proposed to produce an attenuation map by segmenting a (temporary) reconstructed activity image, obtained without attenuation correction. As shown in fig 2, 3 and 6, such an approach is expected to be more successful in SPECT as compared to PET. In PET, regions with zero attenuation that are enclosed in the convex hull, tend to be given a large value when attenuation is ignored. Simple segmentation algorithms will include these regions in the attenuating body, and Tai et al. report that even their sophisticated techniques sometimes fail to separate the arms from the body of the patient [28]. Another possible weakness of their method is that the result of the segmentation is not verified against the original data, so that errors can propagate. In contrast, the MLAA-method repeatedly checks the current estimates against the data. Possibly, the methods could be combined: segmentation of the current activity estimate could result in a useful prior image for the attenuation step, which would accelerate convergence of the attenuation map (and hence also of the activity image). Segmentation errors would be penalized if they resulted in a decrease of the likelihood.

The good results obtained in patient studies of the abdomen and the lower limbs suggests a possible application in whole body imaging. Only a transmission image in the lung region would be required. For the rest of the body, an attenuation map can be produced with MLAA, and the entire whole body study can be reconstructed with attenuation compensation (thus allowing (semi-) quantitative analysis, such as computation of standard uptake values). This would result in a significant decrease of imaging time in e.g. PET oncology studies.

VI. Conclusion

In this paper, a new maximum likelihood method was derived for simultaneous reconstruction of the activity distribution and attenuation map in PET and SPECT. For PET, the MLAA algorithm is composed of existing algorithms for ML reconstruction in emission and transmission tomography. For SPECT, the method combines the existing MLEM algorithm for emission, and a new ML-algorithm which reconstructs the attenuation map, when the attenuated sinogram and the activity distribution are given.
The performance of the algorithm is evaluated using simulations and clinical studies. Good results are obtained in the case of constant attenuation in a (possibly non-convex) attenuating body. For PET, we obtained very good agreement between the MLAA-reconstruction and the image obtained with attenuation correction from a transmission scan, indicating that this approach may be useful for some clinical applications. Simulations suggest that extension to non-uniform attenuation in the lungs may be possible in SPECT, but will be difficult in PET.

VII. Acknowledgments

We wish to thank Stefaan Vleugels and Jan Baetens for their contribution to processing the patient data. We are also grateful to the anonymous reviewers for their valuable comments.

VIII. Appendix A

Ignoring terms not dependent on $\vec{\lambda}$ and $\vec{\mu}$, the log-likelihood function of a SPECT-sinogram, given the activity and attenuation maps is

$$L(\vec{\lambda},\vec{\mu}) = \sum_i \left(-r_i + y_i \ln r_i\right) \quad (12)$$

$$r_i = \sum_j c_{ij} a_{ij} \lambda_j = \sum_j c_{ij} \lambda_j e^{-\sum_\xi l_{i\xi,j}\mu_\xi} \quad (13)$$

where the definition of the symbols is as in the text (equation (6) - (8)). We now derive a gradient ascent algorithm that attempts to maximize $L(\vec{\lambda},\vec{\mu})$ as a function of $\vec{\mu}$. The derivation is similar to that of the reconstruction algorithm for transmission tomography in [22]. The first and second derivatives with respect to the attenuation coefficients equal

$$\frac{\partial L}{\partial \mu_\xi} = \sum_i \left(1 - \frac{y_i}{r_i}\right) q_{i\xi} \quad (14)$$

$$= \sum_i \left(1 - \frac{y_i}{r_i}\right) \left(\sum_k c_{ik} a_{ik} l_{i\xi,k} \lambda_k\right) \quad (15)$$

$$\frac{\partial^2 L}{\partial \mu_\xi \mu_\phi} = \sum_i \left[\left(\frac{y_i}{r_i} - 1\right) \sum_j c_{ij} a_{ij} l_{i\xi,j} l_{i\phi,j} \lambda_j - \frac{y_i\, q_{i\xi}\, q_{i\phi}}{r_i^2}\right]. \quad (16)$$

where $q_{i\xi}$ is defined as in (10). In order to optimize (12), one can compute the update $\Delta\vec{\mu}$ using a quadratic approximation:

$$0 = \left.\frac{\partial L}{\mu_\xi}\right|_{\vec{\mu}+\Delta\vec{\mu}} = \left.\frac{\partial L}{\mu_\xi}\right|_{\vec{\mu}} + \sum_\phi \left.\frac{\partial^2 L}{\partial\mu_\xi \partial\mu_\phi}\right|_{\vec{\mu}} \Delta\mu_\xi \quad (17)$$

$$\mu_\xi^{\text{new}} = \mu_\xi + \Delta\mu_\xi. \quad (18)$$

This implies that $\Delta\vec{\mu}$ should satisfy

$$\sum_\xi \left(\frac{\partial L}{\partial \mu_\xi} + \sum_\phi \frac{\partial^2 L}{\partial\mu_\xi\partial\mu_\phi}\Delta\mu_\xi\right) = 0. \quad (19)$$

The dimensionality of the problem precludes direct computation of $\Delta\vec{\mu}$ from (17). Instead, we estimate $\Delta\vec{\mu}$ as

$$\Delta\mu_\xi = -\frac{\partial L}{\partial \mu_\xi} \Big/ \sum_\phi \frac{\partial^2 L}{\partial \mu_\xi \partial \mu_\phi}. \tag{20}$$

This expression satisfies (19). In addition, for a diagonal Hessian, it reduces to Newton's method. Because the expression is heuristic, there is no advantage in calculating (20) with high precision, so two more approximations are introduced to simplify the computations. First, we assume that $y_i \simeq r_i$ in (16), which is reasonable close to the solution. It also guarantees that the denominator in (20) becomes negative, as required. Second, we replace $\sum_\phi l_{i\phi,j}$ with its upper limit N. Consequently, $\sum_\phi q_{i\phi}$ is replaced by $N\sum_j c_{ij}a_{ij}\lambda_j \simeq N y_i$. Finally, introducing a relaxation factor α_s we obtain

$$\Delta\mu_\xi = \frac{\alpha_s}{N\sum_i q_{i\xi}} \frac{\partial L}{\partial \mu_\xi} = \frac{\alpha_s}{N\sum_i q_{i\xi}} \sum_i \left(1 - \frac{y_i}{r_i}\right) q_{i\xi}. \tag{21}$$

One could directly set $\Delta\mu_\xi$ to $\alpha_s \frac{\partial L}{\partial \mu_\xi}$. However, useful values of α_s would be very dependent on image contents and dimensions. With (21) we attempt to obtain good convergence with α_s close to unity, which is confirmed in our limited experience with the algorithm: useful values are in the range of 1 to 10, relaxation factors about 10 or higher produce oscillations.

IX. Appendix B

The first prior is a probability distribution of absolute attenuation coefficients, the second is a Gibbs distribution favoring locally smooth solutions. To incorporate these priors into the algorithm, the gradient of the logarithm must be added to that of the likelihood function. Since the priors are only a function of $\vec{\mu}$, the update of $\vec{\lambda}$ is not affected.

We define the intensity prior to behave as a Gaussian function with mean $\bar{\mu}_i$ and standard deviation σ_i. In order to combine the Gaussians into a single distribution, the μ-axis is divided in intervals. The values $\bar{\mu}_i$ represent the a-priori expected attenuation coefficients. Additional points t_i are defined as the intersection points of neighboring Gaussians:

$$\frac{1}{\sqrt{2\pi}\sigma_i} \exp \frac{(t_i - \bar{\mu}_i)^2}{2\sigma_i^2} = \frac{1}{\sqrt{2\pi}\sigma_{i+1}} \exp \frac{(t_i - \bar{\mu}_{i+1})^2}{2\sigma_{i+1}^2} \quad \text{and } \bar{\mu}_i < t_i < \bar{\mu}_{i+1}. \tag{22}$$

The Gaussians are combined by defining the gradient of the logarithm M_a as a piecewise linear function:

$$\frac{\partial M_a(\mu|\bar{\mu}_i, i=1..I)}{\partial \mu} = \begin{cases} \frac{\mu - t_{i-1}}{\sigma_i^2} & \text{if } t_{i-1} < \mu \le \frac{t_{i-1}+\bar{\mu}_i}{2} \\ -\frac{\mu - \bar{\mu}_i}{\sigma_i^2} & \text{if } \frac{t_{i-1}+\bar{\mu}_i}{2} < \mu \le \frac{\bar{\mu}_i + t_i}{2} \\ \frac{\mu - t_i}{\sigma_i^2} & \text{if } \frac{\bar{\mu}_i + t_i}{2} < \mu \le t_i \end{cases} \tag{23}$$

where it is assumed that $t_0 = -\infty$ and $t_I = \infty$. Thus, by defining the gradient of the logarithm, (23) defines the prior M_a up to a constant scaling factor, which is irrelevant for the optimization. Consequently, the prior is a continuous function, behaving as a Gaussian near the expected values $\bar{\mu}_i$. Since only the gradient is required, the computations are simple and fast.

To encourage local smoothness, a prior is defined using a Gibbs distribution [8, 19]. The logarithm of the prior M_b is:

$$M_b(\vec{\mu}) = -\sum_{jk} w_{jk} \Phi_\delta(\mu_k - \mu_j) \tag{24}$$

where $w_{jk} = 0$ if pixels j and k are not nearest neighbors, and w_{jk} equals the Euclidean distance between pixels j and k otherwise. We have used an 8-pixel neighborhood. For the function Φ we use a function equivalent to that proposed by Geman and McClure [8], implemented as

$$\Phi_\delta(x) = \frac{x^2}{2\delta^2 + x^2} \tag{25}$$

or (following Mumcuoğlu et al.[19]) the Huber function:

$$\Phi_\delta(x) = \begin{cases} \frac{x^2}{2\delta^2} & \text{if } |x| < \delta \\ \frac{|x| - \delta/2}{\delta} & \text{if } |x| \ge \delta. \end{cases} \tag{26}$$

Both functions converge to the same quadratic form for small x, but the Geman and McClure function is more tolerant than the Huber function for large values of $\mu_k - \mu_j$ and tends to produce sharper edges.

The algorithms (4) and (9) can now be extended with these priors. The gradient of the posterior is the sum of the gradients of the prior and the likelihood. In the denominator, we add the second derivative of the prior to control the step size (expression converges to Newton's method when the prior dominates).

For PET, this leads to

$$\mu_j^{\text{new}} = \mu_j + \alpha_p \frac{\sum_i c_{ij}a_i b_i - \sum_i c_{ij} y_i + \partial M(\vec{\mu})/\partial \mu_j}{N\sum_i c_{ij}a_i b_i - \alpha_p \partial^2 M(\vec{\mu})/\partial \mu_j^2} \tag{27}$$

and for SPECT:

$$\mu_j^{\text{new}} = \mu_j + \frac{\alpha_s}{N\sum_i q_{ij} - \alpha_s \partial^2 M(\vec{\mu})/\partial \mu_j^2} \left[\sum_i q_{ij}\left(1 - \frac{y_i}{\sum_\xi c_{i\xi}a_{i\xi}\lambda_\xi}\right) + \frac{\partial M(\vec{\mu})}{\partial \mu_j}\right] \tag{28}$$

In both equations, $M(\vec{\mu})$ is defined as

$$M(\vec{\mu}) = \beta_a M_a(\vec{\mu}) + \beta_b M_b(\vec{\mu}). \tag{29}$$

As seen from (23), $\partial^2 M_a(\vec{\mu})/\partial \mu_j^2$ is a discontinuous function with value σ_i^{-2} or $-\sigma_i^{-2}$ everywhere, except in the discontinuities, where it is undefined. We arbitrarily define the value at a discontinuity to be that of the interval at its right. A discontinuity in the second derivate may produce an inadequate step size, resulting in oscillations of the gradient ascent

algorithm. However, since the gradient of M_a is directed away from the discontinuity, it tends to drive the solution towards the maxima of M_a, where the prior is well-behaved. We have never observed instability with this approach.
In practice, we replace $\partial^2 M_b(\vec{\mu})/\partial\mu_j^2$ by its upper limit $-1/\delta^2$.

X. REFERENCES

[1] A.V. Bronnikov. "Approximate reconstruction of attenuation map in SPECT imaging." *IEEE Trans Nucl Sci*, vol 42, pp 1483-1488, 1995.

[2] Y. Censor, D.E. Gustafson, A. Lent, H. Tuy. "A new approach to the emission computerized tomography problem: simultaneous calculation of attenuation and activity coefficients." *IEEE Trans Nucl Sci*, vol NS-26, pp 2775-2779, 1979

[3] A. Chatziioannou, M. Dahlbom. "Detailed investigation of transmission and emission data smoothing protocols and their effects on emission images." *IEEE Trans Nucl Sci* vol 43, pp. 290-294, 1996.

[4] N.H. Clinthorne, J.A. Fessler, G.D. Hutchins, W.L Rogers. "Joint maximum likelihood estimation of emission and attenuation densities in PET." *Conf rec of the IEEE Nucl Sci Symposium and Med Imaging Conf.* vol 3, pp 1927-1932, 1991.

[5] H. Erdoğan, J.A. Fessler. "Statistical image reconstruction methods for simultaneous emission/transmission PET scans." *Conf rec of the IEEE Nucl Sci Symposium and Med Imaging Conf.* vol 3, pp 1579-1583, 1996.

[6] J.A. Fessler, E.P. Ficaro, N.H. Clinthorne, K. Lange. "Grouped-coordinate ascent algorithms for penalized-likelihood transmission image reconstruction." *IEEE Trans Med Imaging* vol 16, pp. 166-175, 1997

[7] S. Geman, D. Geman. "Stochastic relaxation, Gibbs distributions, and the Bayesian restoration of images." *IEEE Trans. Pattern Anal. Machine Intell.* vol PAMI-6, pp. 721-741, 1984.

[8] S. Geman, D.E. McClure. "Statistical methods for tomographic image reconstruction." *Bull. Int. Stat. Inst.* vol 52-4, pp. 5-21, 1987

[9] MH Hudson, RS Larkin. "Accelerated image reconstruction using ordered subsets of projection data," *IEEE Trans Med Imaging*, vol 13, pp. 601-609, 1994.

[10] L Kaufman. "Maximum likelihood, least squares and penalized least squares for PET," *IEEE Trans Med Imaging*, vol 12, pp. 200-214, 1993.

[11] A. Krol, S.H. Manglos, J.F. Bowsher, T. Young, D.A. Bassano, F.D. Thomas. "Attenuation compensation in SPECT cardiac imaging using EM-IntraSPECT Method." *J Nucl Med* vol 36, p. 50P, 1995.

[12] K Lange, R Carson. "EM reconstruction algorithms for emission and transmission tomography," *J Comput Assist Tomogr*, vol 8, pp. 306-316, 1984.

[13] Z Liang, R Jaszczak, R Coleman, V Johnson. "Simultaneous reconstruction, segmentation and edge enhancement of relatively piecewise continuous images with intensity-level information." *Med Phys*, vol 18, pp. 394-401, 1991.

[14] Z Liang, J Ye. "Reconstruction of Object-Specific Attenuation Map for Quantitative SPECT," *Proceeding of the 1993 IEEE-MIC*, vol.2, pp 1231-1235, 1994.

[15] S.H. Manglos, T.M. Young, "Constrained IntraSPECT reconstruction from SPECT projections." *Proceeding of the 1993 IEEE-MIC*, pp 1605-1609, 1994.

[16] SR Meikle, M Dahlbom, SR Cherry. "Attenuation correction using count-limited transmission data in positron emission tomography," *J Nucl Med*, vol 34, pp. 143-144, 1993.

[17] C. Michel, A. Bol, A.G. De Volder, A.M Goffinet. "Online brain attenuation correction in PET: towards a fully automated data handling in a clinical environment." *Eur J Nucl Med* vol 15, pp. 712-718, 1989

[18] S.C. Moore, M.F. Kijewski, S.P. Mueller, "A general approach to non-uniform attenuation correction using emission data alone." *J Nucl Med*, vol 38, p 68P, 1997

[19] EÜ Mumcuoğlu, R Leahy, SR Cherry. "Bayesian reconstruction of PET images: methodology and performance analysis," *Phys Med Biol*, vol 41, pp. 1777-1807, 1996.

[20] F. Natterer. "Determination of tissue attenuation in emission tomography of optically dense media." *Inverse Problems*, vol 9, pp 731-736, 1993.

[21] J. Nuyts, P. Dupont, C. Schiepers, L. Mortelmans. "Efficient storage of the detection probability matrix for reconstruction in PET" *J Nucl Med* vol 35, p 187, 1994.

[22] J. Nuyts, B. De Man, P. Dupont, M. Defrise, P. Suetens, L. Mortelmans. "Iterative reconstruction for helical CT: a simulation study." *Phys Med Biol* vol 43, pp 729-737, 1998.

[23] JM Ollinger. "Maximum-likelihood reconstruction of transmission images in emission computed tomography via the EM algorithm," *IEEE Trans Med Imaging*, vol 13, pp. 89-101, 1994.

[24] T.-S. Pan, M.A. King, D.J. de Vries, M. Ljunberg. "Segmentation of the body and lungs from Compton scatter and photopeak window data in SPECT: a Monte Carlo investigation." *IEEE Trans Med Imaging*, vol 15, pp. 13-24, 1996.

[25] P Schmidlin. "Improved iterative image reconstruction using variable projection binning and abbreviated convolution," *Eur J Nucl Med*, vol 21, pp. 930-936, 1994.

[26] LS Shepp, Y Vardi. "Maximum likelihood reconstruction for emission tomography," *IEEE Trans Med Imaging*, vol MI-1, pp. 113-122, 1982.

[27] T.J Spinks, T. Jones, M.C. Gilardi, J.D Heather. "Physical performance of the latest generation of commercial positron scanner." *IEEE Trans Nucl Sci* vol 35, pp. 721-725, 1988

[28] Y.-C. Tai, K.-P. Lin, M. Dahlbom, E.J. Hoffman. "A hybrid attenuation correction technique to compensate for lung density in 3D total body PET." *IEEE Trans Nucl Sci* vol 43, pp. 323-330, 1996

[29] A. Welch, R. Clack, F. Natterer, G.T. Gullberg.

"Toward accurate attenuation correction in SPECT without transmission measurements." *IEEE Trans Med Imaging*, vol 16, pp. 532-541, 1997

[30] M. Xu, P.D. Cutler, W.K. Luk. "Adaptive, segmented attenuation correction for whole-body PET imaging." *IEEE Trans Nucl Sci* vol 43, pp. 331-336, 1996